aerospace

MDPI

Article

Mass and Force Lumping: An Essential Enhancement to the Intrinsic Beam Finite Element Discretization

Jiachen Wang and Zhou Zhou *

School of Aeronautics, Northwestern Polytechnical University, Xi'an 710072, China; jiachen_wang@mail.nwpu.edu.cn
* Correspondence: zhouzhou@nwpu.edu.cn

Abstract: This paper introduces the novel application of the mass and force lumping technique to enhance the finite element discretization of the fully intrinsic beam formulation. In our aeroelastic system model, 2-D unsteady aerodynamics were incorporated alongside simple calculations for thrust and gravity. Through the central difference discretization method, the discretized system was thoroughly examined, shedding light on the advantages of the mass and force lumping approach. With the use of a first-order lumping method, we successfully reconstructed the inertia matrices, external forces, and moments. The resulting equations are more systematically structured, facilitating the extraction of a regular state-space linear system using the direct index reduction method post-linearization. Numerical results further confirm that the proposed techniques can effectively capture the nonlinear dynamics of aeroelastic systems, enabling equation reconstruction and leading to significant benefits in system order reduction and flight dynamical analysis.

Keywords: fully intrinsic equation; geometrically exact beam; differential-algebraic equation; regular state space; mass and force lumping

1. Introduction

High-altitude, long-endurance aircraft often feature large, flexible, high-aspect-ratio wings to enhance aerodynamic efficiency and endurance. Due to the flexibility of the structure and the coupling between the structure and flight dynamics, the large deformations generated during flight are major challenges [1]. In order to understand and safely accommodate these effects in the design process, geometric nonlinear structural effects need to be incorporated into numerical models. For high-altitude, long-endurance aircraft with large flexibility and a high aspect ratio, the geometrically exact beam model proposed by Hodges [2] is one of the most widely used approaches. A number of very flexible aircraft simulation frameworks based on the geometrically exact beam model have been created [3–7], often using nonlinear beam models to represent the structural response, combined with low-order aerodynamic descriptions to reduce coupled nonlinear aeroelastic problems to a manageable scale for time domain calculations. There are several versions of the geometrically exact beam model, such as the displacement-based formulation [8], strain-based formulation [9,10], and fully intrinsic formulation [11,12]. Compared to other formulations, the fully intrinsic beam formulation is characterized by its exclusive reliance on first-order differential equations. Furthermore, it obviates the need to recompute the stiffness and mass matrices after deformation, leading to a marked enhancement in computational efficiency. Consequently, its adoption has become increasingly prevalent in recent times.

Various versions of the fully intrinsic formulation exist, such as the mixed formulation [11], intrinsic beam theory [12,13], and nonlinear modal-based formulation [14,15], among others. While these variations exhibit distinct equation forms, they fundamentally retain the same essence. In modeling aircraft, it is not merely the structural dynamics model

Citation: Wang, J.; Zhou, Z. Mass and Force Lumping: An Essential Enhancement to the Intrinsic Beam Finite Element Discretization. *Aerospace* **2023**, *10*, 957. https://doi.org/10.3390/aerospace10110957

Academic Editor: Hoang-Vu Phan

Received: 27 September 2023
Revised: 31 October 2023
Accepted: 6 November 2023
Published: 13 November 2023

that is paramount; one must also construct models for potential external forces and moments, encompassing aerodynamic force models, gravitational models, thrust, landing gear models, and more. Among these, the establishment of the aerodynamic model is of paramount importance. Its computational speed varies significantly depending on the chosen aerodynamic model, and its accuracy profoundly impacts the precision of the aeroelastic model. Depending on computational accuracy requisites, practitioners often opt for low- to medium-fidelity aerodynamic models. Low-fidelity approaches encompass steady and unsteady strip theory and similar methodologies. In contrast, medium-fidelity strategies include the unsteady vortex lattice method (UVLM) and the unsteady doublet-lattice method (UDLM), to name a few [16]. The selection between these is often predicated upon a balance between the desired accuracy and computational speed.

For the fully intrinsic formulation, there are many forms of spatial discretization, such as the central difference method [17–19], Galerkin approach [3,6,20], and generalized differential quadrature method [21,22], etc. Upon examining the spatial discretization outcomes of the fully intrinsic beam formulation in the aforementioned literature, we discovered that, with the exception of [3], none have delved into the analysis of the system's equation form post spatial discretization. Even when there is a need for linearization, many only go as far as the generalized state space. While [3] recognized the system's equation form as differential-algebraic equations (DAEs), they did not probe further into the results of such an equation form.

While DAEs pose no significant challenges during time domain simulation and static trimming (given that one can employ iterative methods or DAE-specific differential solvers), issues arise when it comes to the system's reduction, dynamic analysis, and control system design for aircraft. The necessity of linearization around equilibrium points results in DAEs manifesting in the form of a generalized state space. The coefficient matrix of its first-order derivative term is singular, rendering the straightforward transformation into a regular state space form quite challenging. This poses considerable complications as compared to linear system equations in the regular state space form, especially when embarking upon tasks like system order reduction, dynamic characteristic analysis, and subsequent control system design. When modeling aircraft systems, it is essential to account for various physical components and their interactions. Assuming an aircraft devoid of lumped masses or concentrated forces and moments is impractical. Key components like payloads, engines, or even landing gears often introduce lumped masses or concentrated forces. In such realistic settings, it becomes impossible to simply dismiss constraint equations from the system. Otherwise, one would introduce the differential of the system input into the governing equations. Such a situation could lead to inaccuracies or even render the system unsolvable under certain conditions. Hence, realistic modeling and proper accounting for these constraints are pivotal for any meaningful aeroelastic or system dynamics analysis.

This study used the mass and force lumping technique as a crucial supplement to the finite element discretization of the fully intrinsic beam formula. After discretizing the partial differential equation using the central difference method, the mass and force lumping method was employed to discretize the system's inertia matrix and external inputs, thereby reconstructing the system's equation structure. After linearizing the system, we utilized a targeted index reduction technique to transform the system from a generalized state space to a regular state space. Subsequently, the static trimming, eigenvalues, and nonlinear time domain simulation results of the system after using mass and force lumping were validated. The results show that the mass and force lumping outcome for the central difference finite element discretization can still capture the nonlinear and dynamic characteristics of the intrinsic beam. Lastly, starting from the regular state space, the modal selection method was used for system model order reduction and dynamic analysis. The remainder of this paper is structured as follows. Section 2 introduces the fully intrinsic beam formulation and the forces and moments that an aircraft might encounter. Section 3, using the central difference finite element method as an example, presents the process of reconstructing the system equation form through mass and force lumping. Section 4 describes how, after system trimming and linearization, a specific index reduction method can be used to convert the generalized state space form of the system equation into a regular state space. In Section 5, numerical examples validate the feasibility and superiority of the method. Finally, Section 6 provides the conclusions and outlook.

2. Aeroelastic System

2.1. Fully Intrinsic Formulation

The fully intrinsic beam equation describes the evolution of velocity measures V, angular velocity measures Ω, internal force measures F, and internal moment measures M at each location s along a beam assembly. The above variables are all three-dimensional vectors defined in the deformed beam cross-sectional B-frame. The y-axis and z-axis of the B-frame are oriented in the directions that define the beam's cross-sectional flexibility and mass coefficients. The x-axis runs along the local tangent of the beam element. Typically, the x-axis points to the right along the span, the y-axis points forward, and the z-axis points upward, as shown in Figure 1. The intrinsic equations are given as [13]

$$F' + (\tilde{k} + \tilde{\kappa})F + f_{external} = \dot{P} + \tilde{\Omega}\, P \tag{1}$$

$$M' + (\tilde{k} + \tilde{\kappa})M + (\tilde{e}_1 + \tilde{\gamma})F + m_{external} = \dot{H} + \tilde{\Omega}H + \tilde{V}\, P \tag{2}$$

$$V' + (\tilde{k} + \tilde{\kappa})V + (\tilde{e}_1 + \tilde{\gamma})\Omega = \dot{\gamma} \tag{3}$$

$$\Omega' + (\tilde{k} + \tilde{\kappa})\Omega = \dot{\kappa} \tag{4}$$

where P, H, κ, γ denote the linear momentum measures, angular momentum measures, force strain measures, and moment strain measures in the B-frame, respectively; $k = [k_1, k_2, k_3]^T$ is the initial curvature of the beam; $e_1 = [1, 0, 0]^T$ is a constant vector; and $f_{external}, m_{external}$ are external forces and moments. $\dot{X}$ indicates the time derivative of X and X' indicates its spatial derivative. $\tilde{X}$ is the cross-product operator. For $X = [X_1, X_2, X_3]^T$,

$$\tilde{X} = \begin{bmatrix} 0 & -X_3 & X_2 \\ X_3 & 0 & -X_1 \\ -X_2 & X_1 & 0 \end{bmatrix} \tag{5}$$

The secondary beam variables P, H, κ, γ are linearly related to the primary variables F, M, V, Ω by the cross-sectional constitutive laws (flexibility and inertia matrices), such that

$$\begin{Bmatrix} \gamma \\ \kappa \end{Bmatrix} = \begin{bmatrix} R & S \\ S^T & T \end{bmatrix} \begin{Bmatrix} F \\ M \end{Bmatrix} = C \begin{Bmatrix} F \\ M \end{Bmatrix} \tag{6}$$

$$\begin{Bmatrix} P \\ H \end{Bmatrix} = \begin{bmatrix} \mu\Delta & -\mu\tilde{\zeta} \\ \mu\tilde{\zeta} & I \end{bmatrix} \begin{Bmatrix} V \\ \Omega \end{Bmatrix} = M \begin{Bmatrix} V \\ \Omega \end{Bmatrix} \tag{7}$$

where, R, S, and T are 3×3 matrices of cross-sectional flexibility coefficients, and μ, ζ, and I are the mass per unit length, mass center offset, and mass moment of inertia per unit length, respectively.

2.2. External Forces and Moments

For aircraft, the trio of fundamental external forces and moments encompasses gravity, aerodynamic force, and thrust. All of these need to be projected onto the B-frame for inclusion in equation computations. Elements marked with a hat indicate concentrated components, while those with an overline denote distributed components. A succinct overview of each is provided below.

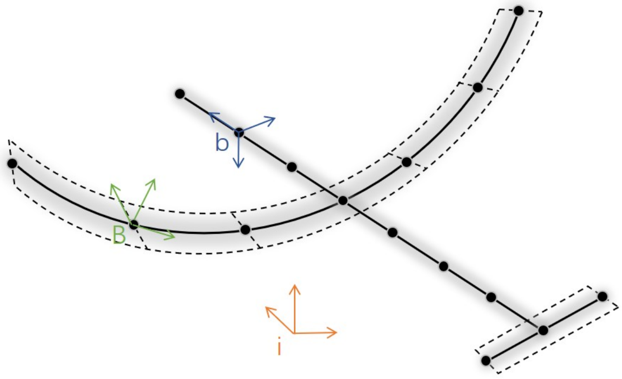

Figure 1. Frame of reference of the intrinsic beam formulation.

2.2.1. Gravity

Initially, we define the inertial reference frame (referred to as the *i*-frame). This frame is recognized as the North–East Earth coordinate system, with its point of origin set at any arbitrary location. Within the *i*-frame, the gravitational vector $g = [0, 0, 9.8]^T$ remains invariant.

Concerning the lumped mass, the external force and moment introduced by gravity in the *B*-frame are articulated as follows:

$$\hat{f}_{gravity} = \hat{\mu} T_{Bi} g \tag{8}$$

$$\hat{m}_{gravity} = \hat{\mu} \tilde{\hat{\zeta}} T_{Bi} g \tag{9}$$

where T_{Bi} represents the coordinate transformation matrix transitioning from the *i*-frame to the *B*-frame, specifically at the lumped mass's location. The term $\hat{\mu}$ denotes the lumped mass, $\hat{\zeta}$ signifies the positional deviation of the lumped mass relative to the beam reference line, and $\hat{I}$ is the matrix capturing the mass moment of inertia of the lumped mass.

The distributed force and moment generated by gravity are as follows:

$$\overline{f}_{gravity} = \mu T_{Bi} g \tag{10}$$

$$\overline{m}_{gravity} = \mu \tilde{\zeta} T_{Bi} g \tag{11}$$

where T_{Bi} denotes the coordinate transformation matrix from the *i*-frame to the *B*-frame.

2.2.2. Aerodynamics

Firstly, we define the aerodynamic frame (denoted as the *a*-frame). The origin of the *a*-frame is positioned at the aerodynamic center of the airfoil, typically at one quarter of the chord length. Within this frame, the *y*- and *z*-axes are established on the airfoil's plane, with the *y*-axis directed forward and the *z*-axis oriented upward. Concurrently, the *x*-axis is aligned with the local tangent of the beam.

Aerodynamic force computations are based on two-dimensional aerodynamics, utilizing specified airfoil parameters such as $C_{l_0}, C_{l_{\delta_e}}, C_{l_\alpha}, C_{d_0}, C_{m_0}, C_{m_{\delta_e}}$, and C_{m_α}. Given these parameters, the velocity and angular velocity at the mid-chord, represented by V_a and Ω_a, are articulated as follows:

$$V_a = T_{aB} V - \tilde{y}_{mc} T_{aB} \Omega \tag{12}$$

$$\Omega_a = T_{aB} \Omega \tag{13}$$

where y_{mc} denotes the position vector from the beam reference axis to the middle chord of the airfoil.

According to Peters 2-D inflow theory [23], the airfoil aerodynamic force and moment can be expressed in the *a*-frame with inflow coefficient λ_0 as

$$f^a_{aero} = \rho b \begin{Bmatrix} 0 \\ -(C_{l_0} + C_{l_\delta}\delta)V_T V_{a_3} + C_{l_\alpha}(V_{a_3} + \lambda_0)^2 - C_{d_0} V_T V_{a_2} \\ (C_{l_0} + C_{l_\delta}\delta)V_T V_{a_2} - C_{l_\alpha}\dot{V}_{a_3} b/2 - C_{l_\alpha} V_{a} 2(V_{a_3} + \lambda_0 - \Omega_{a_1} b/2) - C_{d_0} V_T V_{a_3} \end{Bmatrix} \tag{14}$$

$$m^a_{aero} = \rho b^2 \begin{Bmatrix} (C_{m_0} + C_{m_\delta}\delta)V_T^2 - C_{m_\alpha} V_T V_{a_3} - bC_{l_\alpha}/8 V_{a_2}\Omega_{a_1} - b^2 C_{l_\alpha}\dot{\Omega}^n_{a_1}/32 + bC_{l_\alpha}\dot{V}_{a_3}/8 \\ 0 \\ 0 \end{Bmatrix} \tag{15}$$

The inflow model can be written as

$$\{A_{inflow}\}\dot{\lambda} + (\frac{V_T}{b})\lambda = (-\dot{V}_{a_3} + \frac{b}{2}\dot{\Omega}_{a_1})\{c_{inflow}\} \tag{16}$$

$$\lambda_0 = \frac{1}{2}\{b_{inflow}\}^T\lambda \tag{17}$$

where λ is a column matrix of inflow states, and $\{A_{inflow}\}, \{b_{inflow}\}, \{c_{inflow}\}$ are constant matrices derived in [23].

The distributed force and moment generated by aerodynamics are as follows:

$$\overline{f}_{aero} = T_{Ba} f^a_{aero} \tag{18}$$

$$\overline{m}_{aero} = T_{Ba} m_{aero} + T_{Ba}\tilde{y}_{ac} f^a_{aero} \tag{19}$$

where y_{ac} denotes the position vector from the beam reference axis to the aerodynamic center.

2.2.3. Thrust

For high-altitude, long-endurance aircraft, the thrust units are typically characterized by propellers. In this context, the thrust is simplistically viewed as the result of the thrust magnitude and its associated vector and can be expressed as

$$\hat{f}_{thrust} = f_T(\delta_T)e_f \tag{20}$$

$$\hat{m}_{thrust} = m_T(\delta_T)e_m \tag{21}$$

where e_f and e_m represent the unit vector projections of the thrust force and moment directions within the B-frame, respectively. $f_T(\delta_T)$ and $m_T(\delta_T)$ correspond to the thrust force and moment values produced by the engine in response to the command δ_T, respectively.

2.3. Attitude and Rotation Matrix

Given that the system employs the coordinate transformation matrix from the i-frame to the B-frame during gravity calculations, it is convenient to use Euler angles as state variables. We introduce the body frame (denoted as the b-frame), which has its z-axis directed downward and its x-axis oriented forward within the aircraft's symmetry plane. If the B-frame is appropriately defined, the directional axes of both coordinate systems can only exhibit relationships characterized by axis swapping or axis inversion. For instance, the coordinate transformation matrix transitioning from the B-frame to the b-frame on the wing can be expressed as

$$T_{bB} = \begin{bmatrix} 0 & 1 & 0 \\ 1 & 0 & 0 \\ 0 & 0 & -1 \end{bmatrix} \tag{22}$$

An auxiliary set of equations, elucidating the aircraft's attitude, can be articulated as follows:

$$\begin{Bmatrix} \dot{\hat{\phi}} \\ \dot{\hat{\theta}} \\ \dot{\hat{\psi}} \end{Bmatrix} = \begin{bmatrix} \hat{p} + tan\hat{\theta}(\hat{q}sin\hat{\phi} + \hat{r}cos\hat{\phi}) \\ \hat{q}cos\hat{\phi} - \hat{r}sin\hat{\phi} \\ (\hat{q}sin\hat{\phi} + \hat{r}cos\hat{\phi})/cos\hat{\theta} \end{bmatrix} \tag{23}$$

where $[\hat{\phi}, \hat{\theta}, \hat{\psi}]^T$ denote the Euler angles, and $[\hat{p}, \hat{q}, \hat{r}]^T$ represent the angular velocities. The interrelation between these variables can be articulated as

$$\begin{Bmatrix} \hat{p} \\ \hat{q} \\ \hat{r} \end{Bmatrix} = T_{bB}\hat{\Omega} \tag{24}$$

Defining $\hat{\Phi}$ as $[\hat{\phi}, \hat{\theta}, \hat{\psi}]^T$, Equation (23) can be reformulated as

$$\dot{\hat{\Phi}} = L(\hat{\Phi}, \hat{\Omega}) \tag{25}$$

where L denotes a nonlinear operator.

3. Spatial Time Discretization Scheme

Initially, we utilize Patil's finite element methodology, as delineated in [13], to exemplify the transformation in equation form resultant from mass and force lumping. Subsequently, we provide a concise overview of the equation characteristics post-spatial-discretization and delve into methods for time domain simulation.

3.1. Spatial Finite Element Discretization

To resolve the fully intrinsic beam equations, the beam undergoes discretization into finite elements. This process breaks down the beam into individual beam nodes and beam elements, each element being tethered by two such nodes. Disregarding statically indeterminate structures, the count of nodes in a discretized beam will invariably be one fewer than its corresponding elements. An arbitrary sequencing is used to number the beam nodes and elements. Each side of the given element receives the designation of either Side A or Side B, with their respective node identification numbers duly noted. B-frames are established across all nodes and elements. Pertaining to beam elements, B-frames are set up at each side of the element. As for the beam nodes, their respective B-frames are situated at the node positions, aligning with the B-frame of the element possessing the smallest identification number corresponding to that specific node. It is crucial to note that owing to potential discontinuities in beam inclinations, the B-frame pertaining to the same beam node might vary across different elements.

For each node G, velocity $\hat{V}_G$ and angular velocity $\hat{\Omega}_G$ are articulated within the B-frame. Pertaining to each element n, forces and moments $\hat{F}_A^n, \hat{F}_B^n, \hat{M}_A^n, \hat{M}_B^n$, as well as velocity and angular velocity $V_A^n, V_B^n, \Omega_A^n, \Omega_B^n$ are defined within the B-frame. Notably, for this element n, the identification numbers of its nodes are recognized as A on Side A and B on Side B. Based on this configuration for nodes A, B and element n, the ensuing relationship can be delineated:

$$\hat{V}_A^n = T_{nA}\hat{V}_A,\ \hat{V}_B^n = T_{nB}\hat{V}_B, \tag{26}$$

$$\hat{\Omega}_A^n = T_{nA}\hat{\Omega}_A,\ \hat{\Omega}_B^n = T_{nB}\hat{\Omega}_B \tag{27}$$

Here, T_{nA} and T_{nB} represent the coordinate transformation matrices transitioning from the B-frames of nodes A and B, respectively, to the B-frames located at Side A and Side B of element n. Intrinsically, these matrices are solely predicated upon the beam's initial configuration and the outcome of finite element discretization, remaining unaffected by any subsequent deformations. The state variables F, M, γ, κ pertaining to element n can be discretized as elucidated below:

$$X' = \frac{\hat{X}_B^n - \hat{X}_A^n}{l_n} \tag{28}$$

$$X = \overline{X}^n = \frac{\hat{X}_B^n + \hat{X}_A^n}{2} \tag{29}$$

where l_n denotes the length of element n. State variables V, O, P, H can be discretized as follows:

$$X' = \frac{T_{nB}\hat{X}_B - T_{nA}\hat{X}_A}{l_n} \tag{30}$$

$$X = \overline{X}^n = \frac{\hat{T}_{nB}\hat{X}_B + T_{nA}\hat{X}_A}{2} \tag{31}$$

Substituting Equations (28)–(31) into the intrinsic formula in Equations (1)–(4) yields:

$$\frac{\hat{F}_B^n - \hat{F}_A^n}{l_n} + (\widetilde{\kappa}^n + \widetilde{k}^n)\overline{F}^n + \overline{f}_{external} - \dot{\overline{P}}^n - \widetilde{\overline{\Omega}}^n\overline{P}^n = 0 \tag{32}$$

$$\frac{\hat{M}_B^n - \hat{M}_A^n}{l_n} + (\widetilde{\kappa}^n + \widetilde{k}^n)\overline{M}^n + (\widetilde{e}_1^n + \widetilde{\gamma}^n)\overline{F}^n + \overline{m}_{external} - \dot{\overline{H}}^n - \widetilde{\overline{\Omega}}^n\overline{H}^n - \widetilde{\overline{V}}^n\overline{P}^n = 0 \tag{33}$$

$$\frac{T_{nB}\hat{V}_B - T_{nA}\hat{V}_A}{l_n} + (\widetilde{\kappa}^n + \widetilde{k}^n)\overline{V}^n + (\widetilde{e}_1^n + \widetilde{\gamma}^n)\overline{\Omega}^n - \dot{\overline{\gamma}}^n = 0 \tag{34}$$

$$\frac{T_{nB}\hat{\Omega}_B - T_{nA}\hat{\Omega}_A}{l_n} + (\widetilde{\kappa}^n + \widetilde{k}^n)\overline{\Omega}^n - \dot{\overline{\kappa}}^n = 0 \tag{35}$$

For a given node G, if Side A of the beam elements aligns with node G, it is categorized into the set E_A. Conversely, if Side B of the beam elements corresponds to node G, it is incorporated into the set E_B. Based on this configuration, the subsequent equation can be derived:

$$\sum_{n \in E_A} T_{Gn}\hat{F}_G^n - \sum_{n \in E_B} T_{Gn}\hat{F}_G^n + \hat{f}_{external} - \dot{\hat{P}}_G - \widetilde{\hat{\Omega}_G}\hat{P}_G = 0 \tag{36}$$

$$\sum_{n \in E_A} T_{Gn}\hat{M}_G^n - \sum_{n \in E_B} T_{Gn}\hat{M}_G^n + \hat{m}_{external} - \dot{\hat{H}}_G - \widetilde{\hat{\Omega}_G}\hat{H}_G - \widetilde{\hat{V}_G}\hat{P}_G = 0 \tag{37}$$

Here, T_{Gn} symbolizes the coordinate transformation matrix transitioning from the B-frame of beam element n that aligns with node G to the B-frame specific to node G. Moreover, the equations representing linear momentum and angular momentum are articulated as follows:

$$\begin{Bmatrix} \hat{P}_G \\ \hat{H}_G \end{Bmatrix} = M_G \begin{Bmatrix} \hat{V}_G \\ \hat{\Omega}_G \end{Bmatrix} \tag{38}$$

$$M_G = \begin{bmatrix} \hat{\mu}_G\Delta & -\hat{\mu}_G\tilde{\hat{\zeta}}_G \\ \mu_G\tilde{\hat{\zeta}}_G & \hat{I}_G \end{bmatrix} \tag{39}$$

where $\hat{\mu}_G$ denotes the concentrated mass at node G, $\hat{\zeta}_G$ signifies the positional deviation of the concentrated mass, and $\hat{I}_G$ represents the mass moment of inertia matrix corresponding to the lumped mass at that node.

3.2. Mass and Force Lumping

Mass and force lumping techniques are employed to enhance the system's discretization method. This stands as the primary innovation in this paper. Initially, it is imperative to lump the inertia matrices for all beam elements. For element n and node G, the inertia matrices are as follows:

$$M_n = \begin{bmatrix} \mu_n\Delta & -\mu_n\tilde{\zeta}_n \\ \mu_n\tilde{\zeta}_n & I_n \end{bmatrix}, \; M_G = \begin{bmatrix} \hat{\mu}_G\Delta & -\hat{\mu}_G\tilde{\hat{\zeta}}_G \\ \mu_G\tilde{\hat{\zeta}}_G & \hat{I}_G \end{bmatrix} \tag{40}$$

For an element within the element set E associated with node G, the mass lumping is expressed as

$$M_G^{condense} = M_G + \sum_{n\in E} \begin{bmatrix} T_{nG}^T & O_{3\times3} \\ O_{3\times3} & T_{nG}^T \end{bmatrix} \frac{M_n l_n}{2} \begin{bmatrix} T_{nG} & O_{3\times3} \\ O_{3\times3} & T_{nG} \end{bmatrix} \tag{41}$$

where $M_G^{condense}$ represents the newly lumped inertia matrix corresponding to node G.

Upon completing mass lumping for all beam elements, the mass properties inherent to these elements cease to exist. Consequently, the momentum and angular momentum associated with the beam elements vanish. It becomes crucial to focus on the external forces and moments spread over the beam elements. Drawing from the formulas for gravity, aerodynamic force, and thrust as derived in Equations (10)–(20) for the beam element set E associated with node G, the discretized aerodynamic force and moment directed to node G are expressed as

$$\hat{f}_{aero}^G = \sum_{n\in E} T_{ge} \overline{f}_{aero}^n l_n/2 \tag{42}$$

$$\hat{m}_{aero}^G = \sum_{n\in E} T_{ge} \overline{m}_{aero}^n l_n/2 \tag{43}$$

The distributed gravity is discretized to node G and is expressed as

$$\hat{f}_{gravity}^G = (\hat{\mu}_G + \sum_{n\in E} \mu_n l_n/2) g_G \tag{44}$$

$$\hat{m}_{gravity}^G = (\hat{\mu}_G \widetilde{\hat{\zeta}}_G + \sum_{n\in E} \mu_n \widetilde{\zeta}_n l_n/2) g_G \tag{45}$$

The mass and force lumping techniques utilized in this context are of a straightforward first-order form, and the forces and moments applied are similarly uncomplicated. Readers have the flexibility to incorporate more refined lumping methods and integrate a wider variety of forces and moments, without influencing the outcomes discussed subsequently.

3.3. Final Differential-Algebraic Equations

Following the mass and force lumping process, the equations governing all elements are

$$0 = \frac{\hat{F}_B^n - \hat{F}_A^n}{l_n} + (\widetilde{\kappa}^n + \widetilde{\overline{k}}^n)\overline{F}^n \tag{46}$$

$$0 = \frac{\hat{M}_B^n - \hat{M}_A^n}{l_n} + (\widetilde{\kappa}^n + \widetilde{\overline{k}}^n)\overline{M}^n + (\widetilde{e}_1^n + \widetilde{\gamma}^n)\overline{F}^n \tag{47}$$

$$\dot{\overline{\gamma}}^n = \frac{T_{nB}\hat{V}_B - T_{nA}\hat{V}_A}{l_n} + (\widetilde{\kappa}^n + \widetilde{\overline{k}}^n)\overline{V}^n + (\widetilde{e}_1^n + \widetilde{\gamma}^n)\overline{\Omega}^n \tag{48}$$

$$\dot{\overline{\kappa}}^n = \frac{T_{nB}\hat{\Omega}_B - T_{nA}\hat{\Omega}_A}{l_n} + (\widetilde{\kappa}^n + \widetilde{\overline{k}}^n)\overline{\Omega}^n \tag{49}$$

Additionally, the equations for all nodes are

$$\dot{\hat{P}}_G = \sum_{n\in E_A} T_{Gn}\hat{F}_G^n - \sum_{n\in E_B} T_{Gn}\hat{F}_G^n + \hat{f}_{external} - \widetilde{\hat{\Omega}}_G \hat{P}_G \tag{50}$$

$$\dot{\hat{H}}_G = \sum_{n\in E_A} T_{Gn}\hat{M}_G^n - \sum_{n\in E_B} T_{Gn}\hat{M}_G^n + \hat{m}_{external} - \widetilde{\hat{\Omega}}_G \hat{H}_G - \widetilde{\hat{V}}_G \hat{P}_G \tag{51}$$

$$\dot{\hat{\Phi}}_G = L(\hat{\Phi}_G, \hat{\Omega}_G) \tag{52}$$

When juxtaposed with the state prior to mass and force lumping, it is evident that the equations for beam elements in the fully intrinsic beam formulation no longer encompass external input terms and derivative terms. Therefore, the overarching equations are reconstructed and manifested in a more structured manner. Once linearized, the equations for the beam elements can function as algebraic constraint equations devoid of external input terms and derivative terms, thereby facilitating the application of straightforward index reduction techniques as subsequently described.

3.4. Time Domain Simulation

Equations (46)–(52) can be consolidated and represented in the following form:

$$\dot{x} = f(x) \tag{53}$$

In the time domain simulation, the central difference method is employed. Consequently, Equation (53) can be reformulated as

$$\frac{x(t+\delta t) - x(t)}{\delta t} = \dot{x} = f(x) = \frac{f(x(t+\delta t)) + f(x(t))}{2} \tag{54}$$

Given the current value of the state variables $x(t)$, the Newton–Raphson method can be employed to ascertain the value of the state variables at the subsequent time instant $x(t+\delta t)$ iteratively. As part of the time domain progression for each step, the initial value for $x(t+\delta t)$ is set identically to $x(t)$.

4. Linearization and Index Reduction

4.1. Trimming

To derive linearized outcomes, determining the equilibrium points of Equations (46)–(52) is imperative. For aircraft, equilibrium is typically attained by modifying the control surfaces and throttle commands to stabilize the desired states under specific flight conditions. Consequently, additional equations that pertain to the specified flight conditions are frequently incorporated into the system, exemplified as follows:

$$\begin{cases} V_{ref} = V_{trim} \\ \theta_{ref} = \alpha_{ref} \\ q_{ref} = 0 \end{cases} \tag{55}$$

which indicates that the aircraft maintains level flight at a designated flight speed V_{trim} and specified angle of attack α_{ref}.

For beams with free boundaries, there is no requirement to incorporate boundary conditions, as these conditions are inherently reflected within Equations (50) and (51). When a boundary point is fixed, one should set the corresponding boundary velocity and angular velocity to zero and eliminate the equations pertinent to those variables from Equations (50) and (51).

Upon determining the value of the state variable x at the fixed point using the Newton–Raphson method and subsequently computing the Jacobian matrices for the state variable x and its derivative $\dot{x}$ at said fixed point as Equation (53), a linear generalized state-space form can be derived as follows:

$$E\dot{x} = Ax + Bu \tag{56}$$

where $E = \frac{\partial f}{\partial \dot{x}}|_{x=x_0}$, $A = \frac{\partial f}{\partial x}|_{x=x_0}$, $B = \frac{\partial f}{\partial u}|_{x=x_0,u=u_0}$.

4.2. Index Reduction

While the index reduction method presented here is straightforward, it serves as a vital complement to the mass and force lumping, highlighting its significance. It also represents an innovative aspect of this study. The linearization of Equations (32)–(37) (without mass and force lumping) yields a generalized state space. Upon setting the output as y, this assumes the subsequent form:

$$\begin{cases} E\dot{x} = Ax + Bu \\ y = Cx \end{cases} \tag{57}$$

where E is a singular matrix. Therefore, Equation (57) cannot be transformed into a standard state space form. The generalized state space does not accommodate the methodologies applied to the conventional state space.

Drawing a comparison between Equations (46)–(52) and Equations (32)–(37), it becomes evident that, without mass and force lumping, the first two element equations lack terms for external forces and moments. As a result, the linearization outcome of Equations (46)–(52) emerges as a specific manifestation of the generalized state space. One can reframe the DAEs into two distinct subsystems. The state in these equations bifurcates into two segments: x_d (representing independent states) and x_a (indicative of algebraic states governed by the algebraic constraint). At this juncture, it is pertinent to segment matrices E, A, B, and C accordingly:

$$\begin{aligned} E &= \begin{bmatrix} E_d & E_a \\ 0 & 0 \end{bmatrix} \\ A &= \begin{bmatrix} A_{dd} & A_{da} \\ A_{ad} & A_{aa} \end{bmatrix} \\ B &= \begin{bmatrix} B_d \\ 0 \end{bmatrix} \\ C &= \begin{bmatrix} C_d & C_a \end{bmatrix} \end{aligned} \tag{58}$$

Following this decomposition, the DAEs evolve into the subsequent representation:

$$\begin{cases} E_d\dot{x_d} + E_a\dot{x_a} = A_{dd}x_d + A_{da}x_a + B_d u \\ 0 = A_{ad}x_d + A_{aa}x_a \\ y = C_d x_d + C_a x_a \end{cases} \tag{59}$$

Next, we aim to eradicate the algebraic states. Drawing from the second equation, we can articulate

$$x_a = -A_{aa}^{-1}A_{ad}x_d \tag{60}$$

Substituting this derived expression of x_a into the first and third equation yields

$$\begin{cases} (E_d - E_a A_{aa}^{-1}A_{ad})x_d = (A_{dd} - A_{da}A_{aa}^{-1}A_{ad})x_d + B_d u \\ y = (C_d - C_a A_{aa}^{-1}A_{ad})x_d \end{cases} \tag{61}$$

We arrive at a regular state-space representation as follows:

$$\begin{cases} \dot{x}_d = A'x_d + B'u \\ y = C'x_d \end{cases} \tag{62}$$

where

$$\begin{cases} A' = (E_d - E_a A_{aa}^{-1}A_{ad})^{-1}(A_{dd} - A_{da}A_{aa}^{-1}A_{ad}) \\ B' = (E_d - E_a A_{aa}^{-1}A_{ad})^{-1}B_d \\ C' = (C_d - C_a A_{aa}^{-1}A_{ad}) \end{cases} \tag{63}$$

Consequently, the generalized state space has been transitioned into a regular state-space form with the inclusion of algebraic constraints.

The state variables can be represented as $x = [F_A^{n\,T}, F_B^{n\,T}, M_A^{n\,T}, M_B^{n\,T}, V_G^T, \Omega_G^T, \Phi_G^T]^T$. Equations (46)–(52) can be denoted as $f = [f_{Pe}^T, f_{He}^T, f_{\gamma e}^T, f_{\kappa e}^T, f_{PG}^T, f_{HG}^T, f_{\Phi}^T]^T$.

For the purpose of index reduction, we specifically opt for F_B^n and M_B^n (selecting from either Side A or Side B):

$$\begin{aligned} x_d &= [F_A^{n\,T}, M_A^{n\,T}, V_G^T, \Omega_G^T, \Phi_G^T]^T \\ x_a &= [F_B^{n\,T}, M_B^{n\,T}]^T \\ f_d &= [f_{\gamma e}^T, f_{\kappa e}^T, f_{PG}^T, f_{HG}^T]^T \\ f_a &= [f_{Pe}^T, f_{He}^T]^T \end{aligned} \tag{64}$$

Following the aforementioned procedure, the result is

$$\begin{aligned} &E_d = \frac{\partial f_d}{\partial \dot{x}_d}, E_a = \frac{\partial f_a}{\partial \dot{x}_a} \\ &A_{dd} = \frac{\partial f_d}{\partial x_d}, A_{da} = \frac{\partial f_d}{\partial x_a}, A_{ad} = \frac{\partial f_a}{\partial x_d}, A_{aa} = \frac{\partial f_a}{\partial x_a} \end{aligned} \tag{65}$$

5. Numerical Results

Consider the case of a nonlinear aeroelastic flying wing. This particular aircraft model was previously employed in studies conducted by Patil and Hodges [13], subsequently by Su [9], and further explored by Wang [14], as depicted in Figure 2. The aircraft's properties are delineated in Table 1. In this study, the merits of the mass and force lumping method, as well as the index reduction method, will be elucidated through the numerical outcomes associated with the flying wing. Furthermore, these numerical results will undergo validation against the flexible dynamic model presented in the established literature.

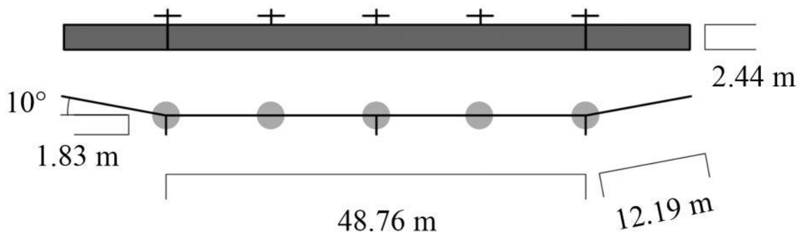

Figure 2. The geometry of the flying wing, as referenced in [9,13,14].

Table 1. Relevant properties of the flying wing [13].

Parameter	Value
Elastic/reference axis	25% chord
Aerodynamic center	25% chord
Center of gravity	25% chord
GJ	1.65×10^5 N·m^2
EI_2	1.03×10^6 N·m^2
EI_3	1.24×10^7 N·m^2
m	8.93 kg/m
I_{11}	4.15 kg·m
I_{22}	0.69 kg·m
I_{33}	3.46 kg·m
Wing C_{l_α}	2π
Wing C_{l_δ}	1
Wing C_{d_0}	0.01
Wing C_{m_0}	0.025
Wing C_{m_δ}	−0.25
Pod C_{l_α}	5
Pod C_{d_0}	0.02
Pod C_{m_0}	0

For the designated aircraft, the elevator and aileron, denoted as δ_e and δ_a, respectively, span the entire wing length, as illustrated in Figure 3. In the example aircraft, the structure exhibits a span of 73.14 m with a consistent chord of 2.44 m. It is partitioned into six sections by its propellers, and each terminal span possesses a dihedral angle of 10 degrees. Beneath the wing, there are three pods that act as the landing gear or bay for payload. Each of these pods measures 1.83 m in length. The payload is positioned at the central location of the middle pod, with weights between 0 kg and 227 kg.

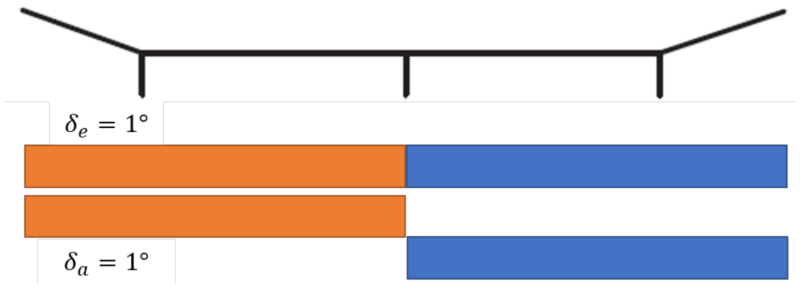

Figure 3. The elevator δ_e and aileron δ_a of the flying wing.

First, discretize the aircraft using finite element methods. For each section on the wing, divide it into four beam elements and five beam grids. For every pod beneath the wing, segment it into two beam elements and three beam grids. Subsequently, employ Equations (40)–(45) on all beam elements for mass and force lumping. Finally, by applying Equations (46)–(52) to all beam elements and grids, we can derive the final differential-algebraic equations for the aircraft.

5.1. Trim Results

Use Equation (55) to trim the aircraft for level flight at a speed of 12.2 m/s. The payload at the aircraft central pod varies from 0 kg to 227 kg, corresponding to a range of 0% to 100%. Refer to Figure 4 for the trim results. Comparisons are made with the works of Patil [13] and Su [9]. It can be seen that after using the mass and force lumping described above, the trim results are essentially the same.

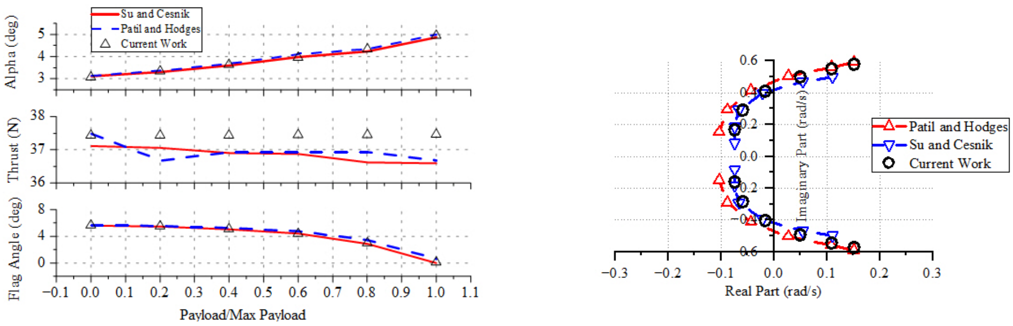

(**a**) Angle of attack, thrust, and flap deflection (**b**) Root locus

Figure 4. Trimming results of the flexible flying wing with payload varying from 0 to 227 kg. (**a**) Angle of attack, thrust, and flap deflection. (**b**) Root locus. The format of the comparison figure is similar to that of Wang [14].

5.2. Nonlinear Time Domain Simulation

The input curve shown in Figure 5a is utilized for subsequent linear and nonlinear time domain simulations. Unless otherwise specified, the input curve remains unchanged, with only the input peak values being modified. In this section, the peak value for elevator δ_e is set to 5 degrees. Results from the current study, using 100% payload, are compared with those from Patil's research [13].

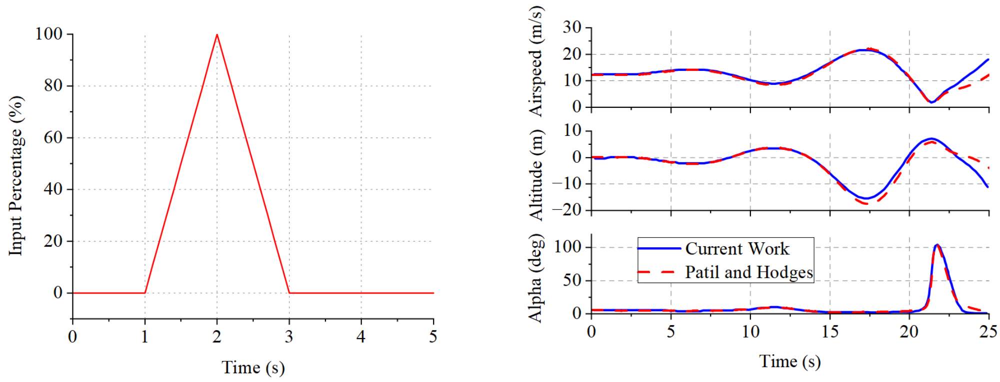

(**a**) The input curve (**b**) Nonlinear time domain simulation results

Figure 5. (**a**) The percentage of input curve; (**b**) nonlinear time domain simulation results with δ_e input with a peak value of 5 degrees.

The results prior to 20 s show good agreement. However, the outcomes after 20 s are not considered reliable as the angle of attack surpasses 100 degrees, and the model does not account for stall conditions.

5.3. Linearization and Index Reduction

Examining Patil's findings [13], it is evident that they are in a generalized state-space form after linearization. Transforming this system into a regular state-space form presents challenges. Conversely, the above-described method of index reduction and linearization in Equations (57)–(65) facilitates the straightforward acquisition of linearization results in a standard state-space form. The eigenvalues of the state space are illustrated in Figure 6. When juxtaposed with the results without mass and force lumping, as well as index reduction, the eigenvalues remain consistent. This affirms that the dynamic characteristics of the system remained unchanged after the mass and force lumping.

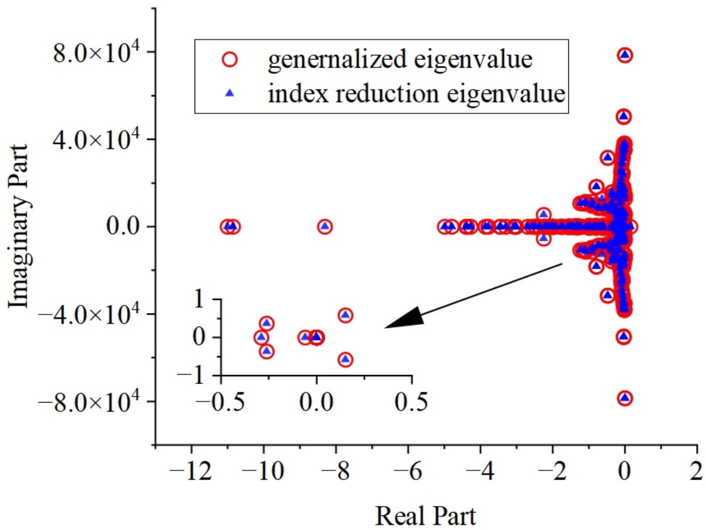

Figure 6. Comparison of eigenvalues before and after mass and force lumping, where the part indicated by the arrow represents the distribution of the eigenvalues near the origin.

Utilizing the input curve from Figure 5a and employing the peak values of δ_e and δ_a at 2 degrees and 10 degrees, respectively, for longitudinal and lateral directional simulations, the time domain simulation results are as depicted in Figure 7. When contrasting the linear system with its nonlinear counterpart, certain observations can be made. For the longitudinal system, as illustrated in Figure 7a, the linearization outcomes align closely with the nonlinear simulation results when near the equilibrium state. However, post 10 s, the system substantially deviates from equilibrium, leading to marked discrepancies. The lateral result in Figure 7b, on the other hand, consistently shows good agreement throughout due to its proximity to the equilibrium state.

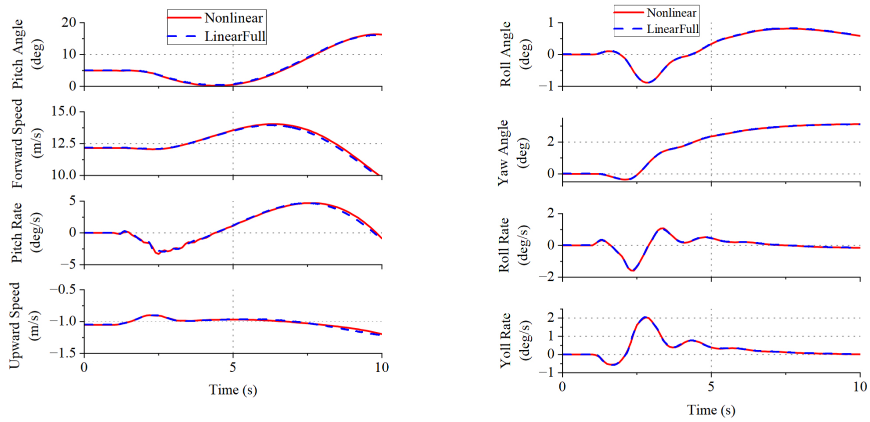

(**a**) Longitudinal results (**b**) Lateral results

Figure 7. Comparison of linear and nonlinear time domain simulation results in (**a**) longitudinal direction and (**b**) lateral direction with peak values of δ_e and δ_a at 2 degrees and 10 degrees, respectively.

5.4. Model Order Reduction

In actual flight conditions, the aerodynamic loads and inherent structural characteristics of an aircraft contribute to enhanced damping effects at high frequencies. As a result, model order reduction is achieved by selecting eigenvalues and eigenvectors near the origin, which is called the eigenvalue selection method. The selected eigenvalues are represented in Figure 8.

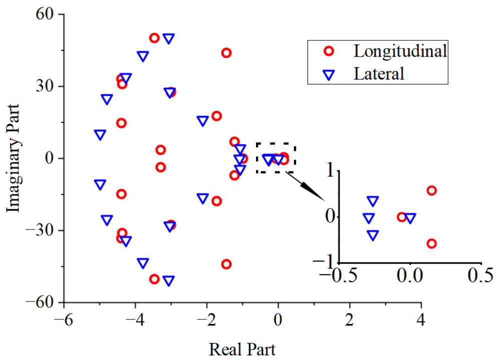

Figure 8. Eigenvalues selected from Figure 6 to execute model reduction, where the part indicated by the arrow represents the distribution of the eigenvalues near the origin.

We designate δ_e as the input for longitudinal dynamics and da for lateral dynamics. The longitudinal outputs comprise the pitch angle, forward velocity, upward velocity, and center-bending moment at the central position. The lateral outputs encompass the roll angle, yaw angle, roll speed, and yaw speed at the central position. The outputs selected here are reference quantities that best reflect the current state of the aircraft during flight dynamics analysis. The Bode plots for the longitudinal and lateral responses are presented in Figures 9 and 10, respectively.

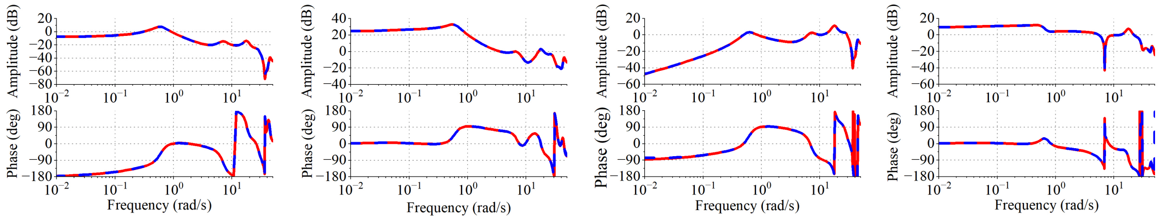

(**a**) *ds* to pitch angle (**b**) *ds* to forward speed (**c**) *ds* to pitch rate (**d**) *ds* to upward speed

Figure 9. Comparison of Bode plots from *ds* to (**a**) pitch angle, (**b**) forward speed, (**c**) pitch rate, and (**d**) upward velocity before and after model reduction. The red lines represent the full-order system, while the blue lines represent the reduced-order system.

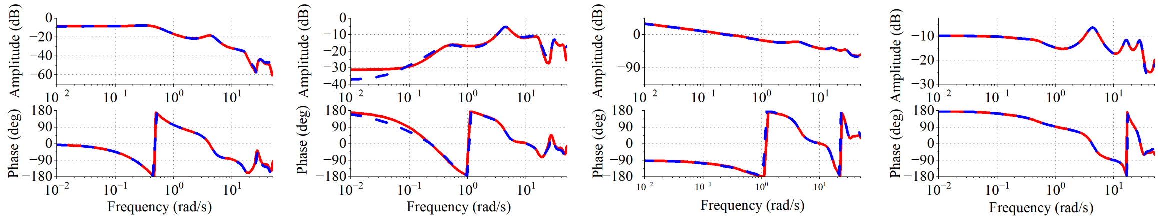

(**a**) *da* to roll angle (**b**) *da* to roll rate (**c**) *da* to yaw angle (**d**) *da* to yaw rate

Figure 10. Comparison of Bode plots from *da* to (**a**) roll angle, (**b**) roll rate, (**c**) yaw angle, and (**d**) yaw rate before and after model reduction. The red lines represent the full-order system, while the blue lines represent the reduced-order system.

As can be observed from the figures, the reduced-order model, with the exception of the Bode plot corresponding to δ_a to the roll rate in its lower-frequency segment, aligns exceptionally well with the full-order model over a frequency range of 10^{-2} to 10^2. The discrepancies arise likely due to the omission of certain low-frequency eigenvalues with real parts far from the origin during eigenvalue selection. This necessitates a trade-off between reduction accuracy and the number of reduced-order terms.

A comparison of the time domain simulation results between the reduced-order system and the full-order system is shown in Figure 11. The time domain simulation results are in complete agreement and align consistently with the frequency domain characteristics.

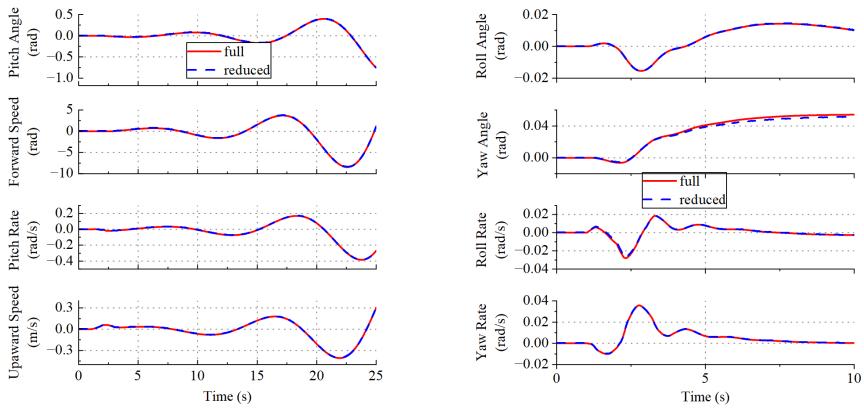

(**a**) Longitudinal time domain simulation (**b**) Lateral time domain simulation

Figure 11. Comparison of reduced-order and full-order linear time domain simulation in (**a**) longitudinal direction and (**b**) lateral direction.

When contrasted with the widely used balanced reduction method, the eigenvector of the reduced-order system encapsulates all the system's characteristic motions. This facilitates the analysis of the impact of each mode. The eigenvector linked to each actual eigenvalue and each set of complex eigenvalues relates solely to the eigenvector corresponding to the same eigenvalue in the original system. This retains tangible physical relevance and offers valuable insights for flight dynamics analysis, as well as for the assessment of controllability and observability.

5.5. Analysis of Flight Dynamics

The model reduction technique discussed previously preserves the modal data of the full-order linear model. Figures 12 and 13 display the first four modal responses of the longitudinal and lateral reduced-order models, respectively. The first row represents the velocity outcomes, while the second row illustrates the internal moment results.

It can be observed that both pure rigid body motion modes and structural modal forms are absent in flexible aircraft. All modes are composites of motion and structural modalities. A single type of structural mode may correspond to multiple eigenvalues. For instance, the second and third modes in the longitudinal direction both reflect the first-order symmetric bending mode to some extent. Similarly, the first and third modes in the lateral directional domain capture the first-order anti-symmetric bending mode.

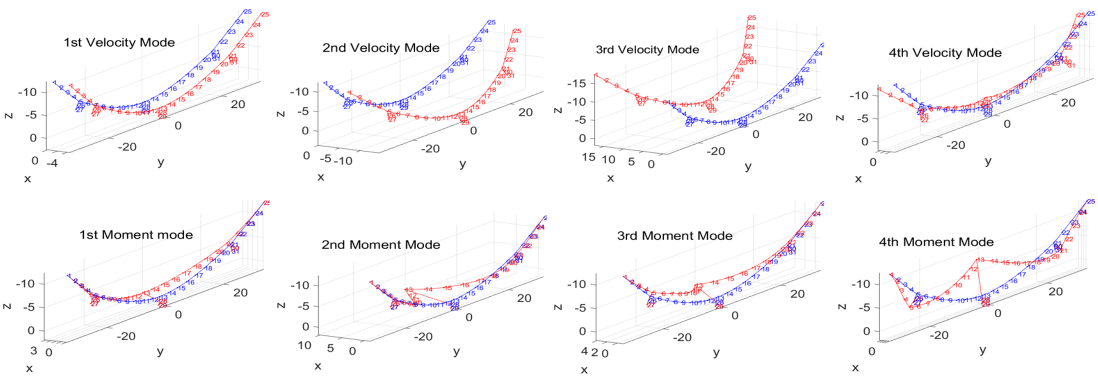

Figure 12. From left to right are the first four modes of longitudinal reduced-order model. The blue lines represent the shape of the aircraft, while the red lines represent the shape of the eigenvector.

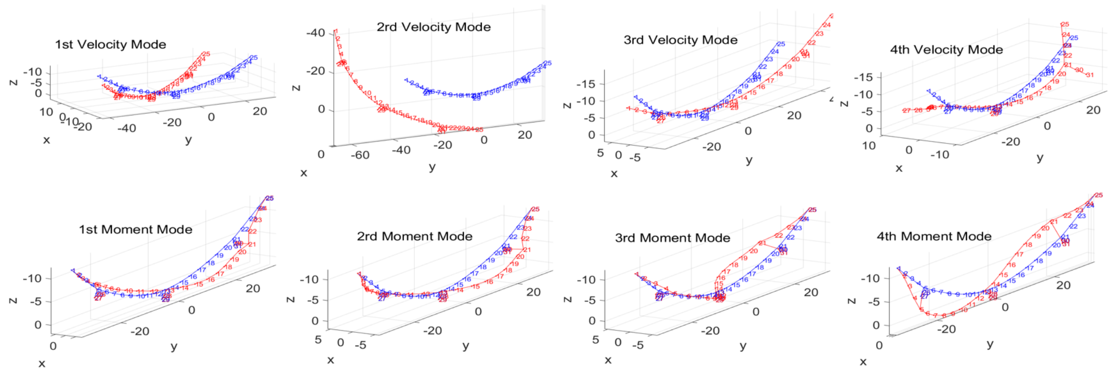

Figure 13. From left to right are the first four modes of the lateral reduced-order model. The blue lines represent the shape of the aircraft, while the red lines represent the shape of the eigenvectors.

Given that the reduced-order system maintains the dynamic modes of the original system, the contribution values of various states can be distinguished during the simulation of the reduced-order model. Moreover, they can be linearly superimposed. The modal contributions are depicted in Figure 14. Within the figure, the lines delineated by red circles represent the output of the reduced-order system, while the remaining lines illustrate the contribution of each individual mode. This is an aspect that the balanced reduction method cannot achieve, as its eigenvalues no longer retain the physical characteristics of the original system. Through evaluating the contributions of each eigenvector under distinct excitations, we can examine the aircraft's dynamic behaviors and determine the proportional contributions of different modes to the aircraft's overall dynamic response.

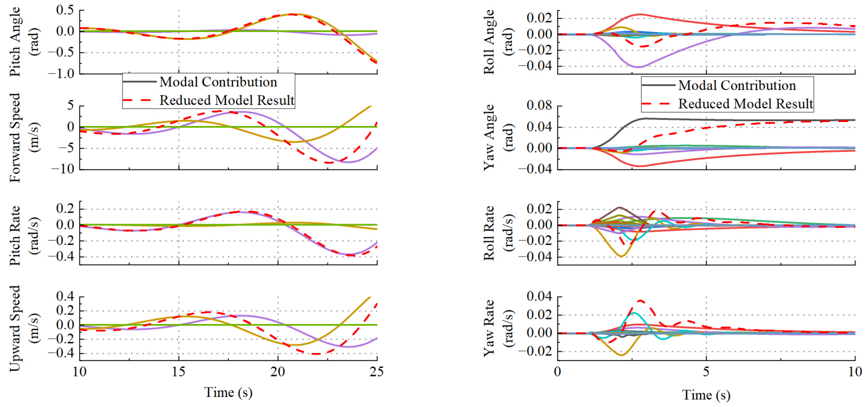

(**a**) Longitudinal modal contributions (**b**) Lateral modal contributions

Figure 14. The dashed lines represent the time-domain simulation results for the reduced-order system, while the solid lines depict modal contributions of several main modes in (**a**) longitudinal direction and (**b**) lateral direction.

6. Conclusions and Future Works

In this study, we introduce the concept of employing the mass and force lumping technique as a vital enhancement to the finite element discretization of the fully intrinsic beam formulation. Using the central difference discretization method as a demonstration, we systematically analyzed the form of the discretized system equations, elucidating the fundamental principles of employing the mass and force lumping technique. After reconstructing the inertia matrices as well as external forces and torques in the discretized fully intrinsic beam formulation using the first-order mass and force lumping method, we observed that the restructured equations possess a more structured form. This form can subsequently be transformed into a regular state space through the application of the index reduction method.

Subsequently, we leveraged a widely referenced, high-aspect-ratio flying wing configuration as a case study for numerical verification. After discretizing the system using the finite element method integrated with the mass and force lumping technique described earlier, we computed the trim results and long-period eigenvalues of the system under various payloads. Comparing these with results from the literature, we found a substantial degree of alignment. Additionally, we compared the eigenvalues of the system before and after applying the mass and force lumping technique, noting that there was no change in the system's eigenvalues. This affirmed that the dynamic characteristics of the system remained unchanged after the mass and force lumping. Lastly, we employed an eigenvalue selection method to reduce the system's order, verifying the accuracy of the reduced system and analyzing the dynamic characteristics of the original system based on it. The eigenvalue selection method can only be implemented in a regular state space, further attesting to the efficacy of mass and force lumping.

Since mass and force lumping do not disrupt the finite element discretization process, in future works, we intend to apply more precise lumping methods to an array of finite element discretization techniques, such as the Galerkin approach and the generalized differential quadrature method. Our goal is to reconstruct the equations and further validate the extensive application prospects of mass and force lumping, thereby expanding the application boundaries of these finite element discretization methods.

Author Contributions: Conceptualization, J.W. and Z.Z.; methodology, J.W.; software, J.W.; validation, J.W.; formal analysis, J.W.; investigation, J.W.; writing—original draft preparation, J.W.; writing—review and editing, J.W. All authors have read and agreed to the published version of the manuscript.

Funding: This research was funded by the ND Basic Research Funds (G2022WD), Foundation Enhancement Program (2021-JCJQ-JJ-0790 and 2022-JCJQ-JJ-1137), and Natural Science Basic Research Program of Shaanxi (2023-JC-YB-010).

Data Availability Statement: Not applicable.

Conflicts of Interest: The authors declare no conflict of interest.

References

1. Cesnik, C.E.; Palacios, R.; Reichenbach, E.Y. Reexamined structural design procedures for very flexible aircraft. *J. Aircr.* **2014**, *51*, 1580–1591. [CrossRef]
2. Hodges, D.H. A mixed variational formulation based on exact intrinsic equations for dynamics of moving beams. *Int. J. Solids Struct.* **1990**, *26*, 1253–1273. [CrossRef]
3. Liang, J.; Bai, J.; Sun, Z.; Wang, H.; Zhang, B.; Chang, M. Modeling and analysis of a geometrically nonlinear joined wing under thrust force. *J. Sound Vib.* **2023**, *544*, 117369. [CrossRef]
4. Dehadrai, A.R.; Sharma, I.; Gupta, S.S. Transient planar dynamics of cable-payload systems using geometrically exact beam theory. *Int. J. Mech. Sci.* **2022**, *224*, 107271. [CrossRef]
5. Moravej Barzani, S.H.; Shahverdi, H.; Amoozgar, M. Nonlinear aeroelastic stability analysis of a two-stage axially moving telescopic wing by using fully intrinsic equations. *Proc. Inst. Mech. Eng. Part G J. Aerosp. Eng.* **2022**, *236*, 3102–3110. [CrossRef]
6. Chen, L.; Hu, X.; Liu, Y. Space-Time Finite Element Method for Fully Intrinsic Equations of Geometrically Exact Beam. *Aerospace* **2023**, *10*, 92. [CrossRef]
7. Shang, L.; Xia, P.; Hodges, D.H.; Lin, C. Geometrically Exact Beam-Based Aeroelastic Modeling and Solution of Composite Rotor Blades in Forward Flight. *J. Am. Helicopter Soc.* **2023**, *68*, 127–142. [CrossRef]
8. Patuelli, C.; Cestino, E.; Frulla, G. A Beam Finite Element for Static and Dynamic Analysis of Composite and Stiffened Structures with Bending-Torsion Coupling. *Aerospace* **2023**, *10*, 142. [CrossRef]
9. Su, W.; Cesnik, C.E. Dynamic response of highly flexible flying wings. *AIAA J.* **2011**, *49*, 324–339. [CrossRef]
10. Riso, C.; Cesnik, C.E.S. Impact of Low-Order Modeling on Aeroelastic Predictions for Very Flexible Wings. *J. Aircr.* **2022**, *60*, 662–687. [CrossRef]
11. Patil, M.J.; Hodges, D.H.; Cesnik, C.E. Nonlinear aeroelasticity and flight dynamics of high-altitude long-endurance aircraft. *J. Aircr.* **2001**, *38*, 88–94. [CrossRef]
12. Moshtaghzadeh, M.; Izadpanahi, E.; Bejan, A.; Mardanpour, P. Evolutionary Aeroelastic Design of Flying-Wing Cross Section. *AIAA J.* **2022**, *60*, 913–924. [CrossRef]
13. Patil, M.J.; Hodges, D.H. Flight dynamics of highly flexible flying wings. *J. Aircr.* **2006**, *43*, 1790–1799. [CrossRef]
14. Wang, Y.; Wynn, A.; Palacios, R. Nonlinear modal aeroservoelastic analysis framework for flexible aircraft. *AIAA J.* **2016**, *54*, 3075–3090. [CrossRef]
15. Qi, P.; Zhao, X. Flight Control for Very Flexible Aircraft Using Model-Free Adaptive Control. *J. Guid. Control. Dyn.* **2020**, *43*, 608–619. [CrossRef]
16. Afonso, F.; Vale, J.; Oliveira, É.; Lau, F.; Suleman, A. A review on non-linear aeroelasticity of high aspect-ratio wings. *Prog. Aerosp. Sci.* **2017**, *89*, 40–57. [CrossRef]
17. Syed, A.A.; Moshtaghzadeh, M.; Hodges, D.H.; Mardanpour, P. Aeroelasticity of Flying-Wing Aircraft Subject to Morphing: A Stability Study. *AIAA J.* **2022**, *60*, 5372–5385. [CrossRef]
18. Sotoudeh, Z.; Hodges, D.H. Modeling beams with various boundary conditions using fully intrinsic equations. *J. Appl. Mech.* **2011**, *78*, 031010. [CrossRef]
19. Sotoudeh, Z.; Hodges, D.H. Incremental method for structural analysis of joined-wing aircraft. *J. Aircr.* **2011**, *48*, 1588–1601. [CrossRef]
20. Patil, M.J.; Althoff, M. Energy-consistent, Galerkin approach for the nonlinear dynamics of beams using intrinsic equations. *J. Vib. Control* **2011**, *17*, 1748–1758. [CrossRef]
21. Amoozgar, M.; Shahverdi, H.; Nobari, A. Aeroelastic stability of hingeless rotor blades in hover using fully intrinsic equations. *AIAA J.* **2017**, *55*, 2450–2460. [CrossRef]
22. Chen, L.; Liu, Y. Differential Quadrature Method for Fully Intrinsic Equations of Geometrically Exact Beams. *Aerospace* **2022**, *9*, 596. [CrossRef]
23. Peters, D.A.; Karunamoorthy, S.; Cao, W.M. Finite state induced flow models. I-Two-dimensional thin airfoil. *J. Aircr.* **1995**, *32*, 313–322. [CrossRef]